

## *A Small Magnetically Shielded Motor Assembly Design Example*

By: Steve Mowry, President  
SM Audio Engineering Consulting Co.

Many times in my career as a transducer engineer, I have been asked to improve and/or modify an existing transducer design. With respect to engineering simulation software tools, this is where they can be very powerful. We can reduce the problem to a better/worse scenario and we have a baseline design to which we can compare and contrast our simulation results. This is essentially how we shall proceed in the following design example.

### **VOICE COIL DESIGN**

Usually, our first step in designing any motor assembly is to design a suitable voice coil. Typically, a major consideration in voice coil design is to comply with the specifications for the DC resistance of the voice coil at  $25\text{ }^{\circ}\text{C} \pm 5\%$ ,  $R_c(25)$ , wind height, mass, inside diameter (ID) and outside diameter (OD). This process can be facilitated through the use of a spreadsheet computer program containing lookup tables and formulas written into 'cells'. Every transducer engineer seems to have his own. For this example we shall select a small but commonly available voice coil inside diameter of 0.52 in. (13.2 mm) and flat aluminum magnet wire for low voice coil mass. The output from my voice coil worksheet is shown below in figure 1.

<b>Flat Wire Voice Coil Design</b>		<b>Input Parameters</b>	
<i>(units are ohms, inches, and grams)</i>		<b>Packing Factor</b>	<b>0.946</b>
<b>DC Resistance@25C</b>	<b>= 2.75 ohms</b>	<b>DC Resistance@25C</b>	<b>2.75</b>
<b>Conductor Width</b>	<b>= 0.0140 in</b>	<b>Wire Width</b>	<b>0.0150</b>
<b>Conductor Thickness</b>	<b>= 0.0030 in</b>	<b>Wire Thick</b>	<b>0.0040</b>
<b>Voice Coil ID</b>	<b>= 0.5200 in</b>	<b>Wire Insulation Thk</b>	<b>0.0005</b>
<b>Conductive Area Fact</b>	<b>= 0.703</b>	<b>Bobbin Thick</b>	<b>0.0020</b>
<b>Length of Conductor</b>	<b>= 101.7 in</b>	<b>Bobbin Adhesive Thk</b>	<b>0.0005</b>
<b>Avg. Conductive Dia</b>	<b>= 0.5400 in</b>	<b>Voice Coil ID</b>	<b>0.5200</b>
<b>Coil Outside Diameter</b>	<b>= 0.5550 in</b>		
<b>Number of Turns</b>	<b>= 60.0</b>		
<b>Wind Height</b>	<b>= 0.254 in</b>		
<b>Stacking Factor</b>	<b>= 0.629</b>		
<b>Total Wire Mass</b>	<b>= 0.261 g</b>		
<b>Mass of Adhesive</b>	<b>= 0.012 g</b>		
<b>Total Mass w/o Bobbin</b>	<b>= 0.273 g</b>		
		<b>TYPE</b>	<b>RHO</b>
		<b>Flat Wire</b>	<b>Al 1.1142 E-6</b>

**Figure 1. Output from the Voice Coil Spreadsheet.**

The voice coil defined above utilizes a single layer of rectangular aluminum magnet wire with a polyester/polyimide insulation system and a thermoplastic polyamide/polyimide adhesive bond coat, Thermal Class 180 °C or better. The voice coil bobbin can be anodized aluminum or Kapton (polyimide) and is 2.0 mil thick. This voice coil was chosen for example purposes only. Almost any type of voice coil could be utilized in the motor geometries that will be investigated.

### **DC ANALYSAIS**

This transducer design project has been specified to be nominally 2 in. (50 mm) with regards to the squared basket flange's overall width and length. This puts a constraint on the outside diameter of the motor assembly and this transducer must also be magnetically shielded for potential multimedia applications. With respect to these design requirements, we shall now select our magnet material,

Ceramic 8. Let's look at the properties of this low cost ferrite based magnet material. Figure 2 below illustrates the BH curve for Ceramic 8 magnet material at 25 °C. The units for the Flux Density, **B**, and Field Strength, **H**, are T (Tesla) and Am<sup>-1</sup> (Amperes per meter) respectively. This graphic representation of the BH curve file is an important input to our finite element model that defines the magnets' DC characteristics.

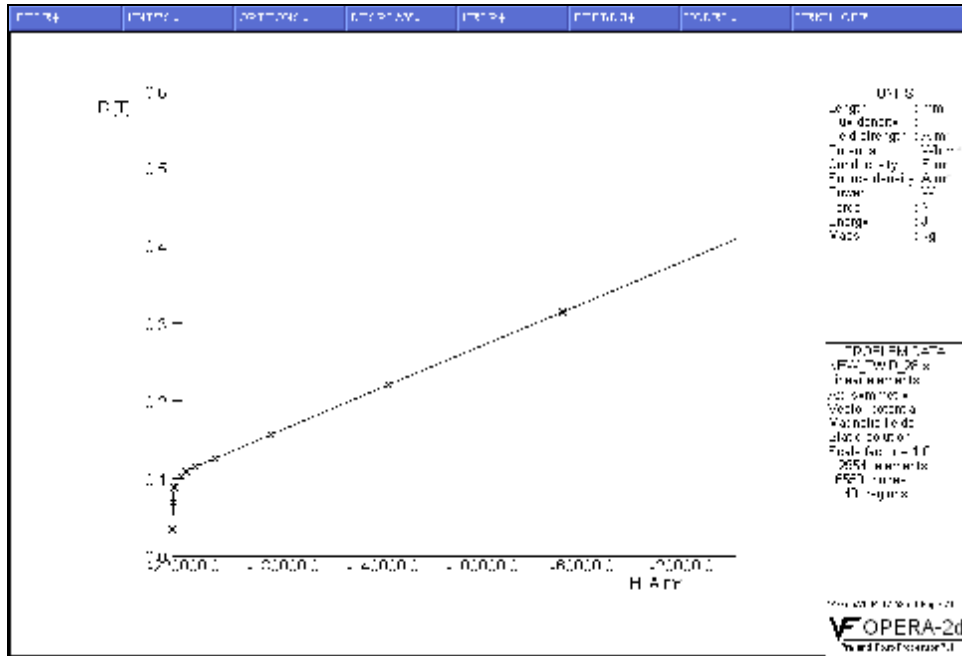


**Figure 2. BH Curve for typical Ceramic 8 Magnets at 25 °C.**

Additional BH curve input files are required to define the DC characteristics of 1010 steel, copper and air. In our DC models, copper and air have identical behavior; however, we shall subsequently see that copper and air within the proximity of the voice coil behave very differently when an AC signal is applied to the voice coil. The BH curves for 1010 steel and air/copper are illustrated below in figures 3 and 4 respectively.

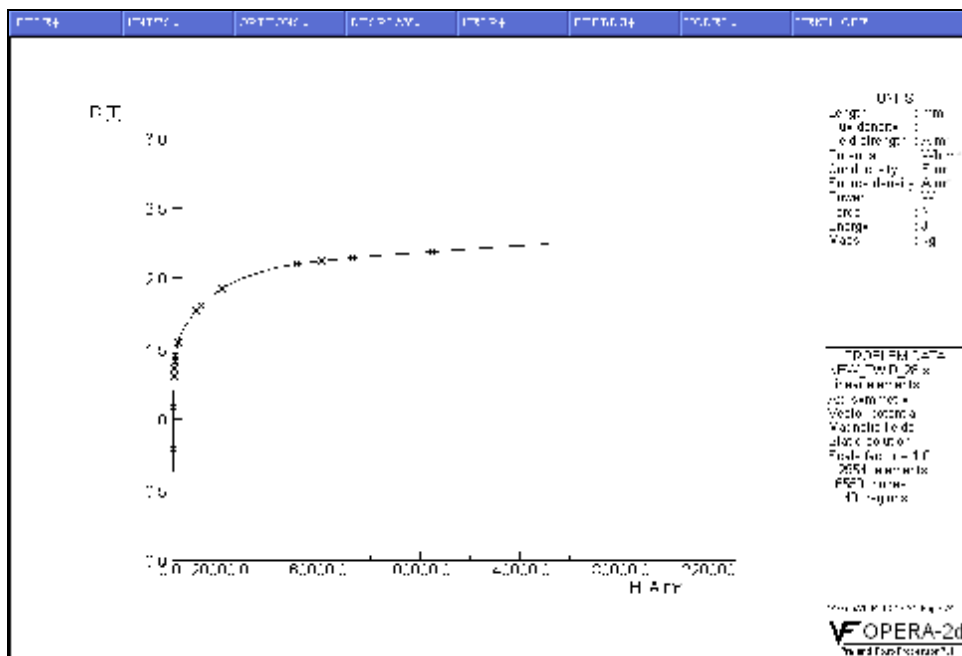


**Figure 3. BH Curve for 1010 Steel at 25 °C.**

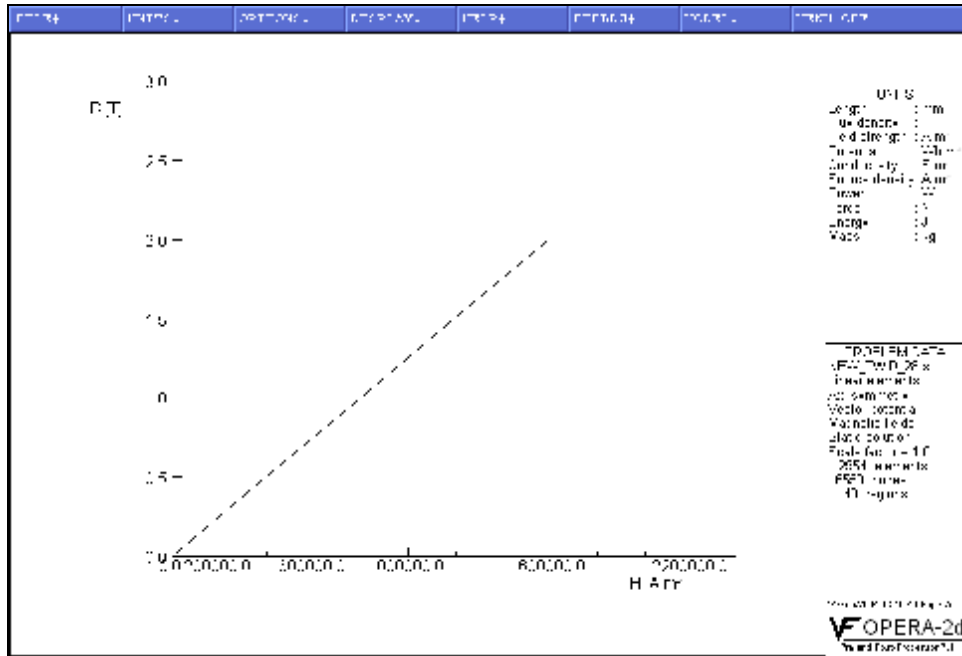


**Figure 4. The BH Curve for air and all other nonferrous materials.**

Our next step is to create the axi-symmetric geometry inside the software’s pre-processor. The geometry can also be imported and/or exported in a \*.dxf file format. We will utilize VECTOR FIELDS OPERA 2d for all electromagnetic finite element analysis. Let’s start with a commonly used geometric configuration for a shielded motor assembly. Figure 5 below illustrates the geometry and solution to our first DC finite element model. A portion of the stamped steel basket is included in the models and we shall see the basket does play a role in the electromagnetic behavior of the motor assemblies.

**Magnetic Flux Density  $|B(r,z)|$  with the Flux Lines ( $r \times$  Magnetic Vector Potential)**

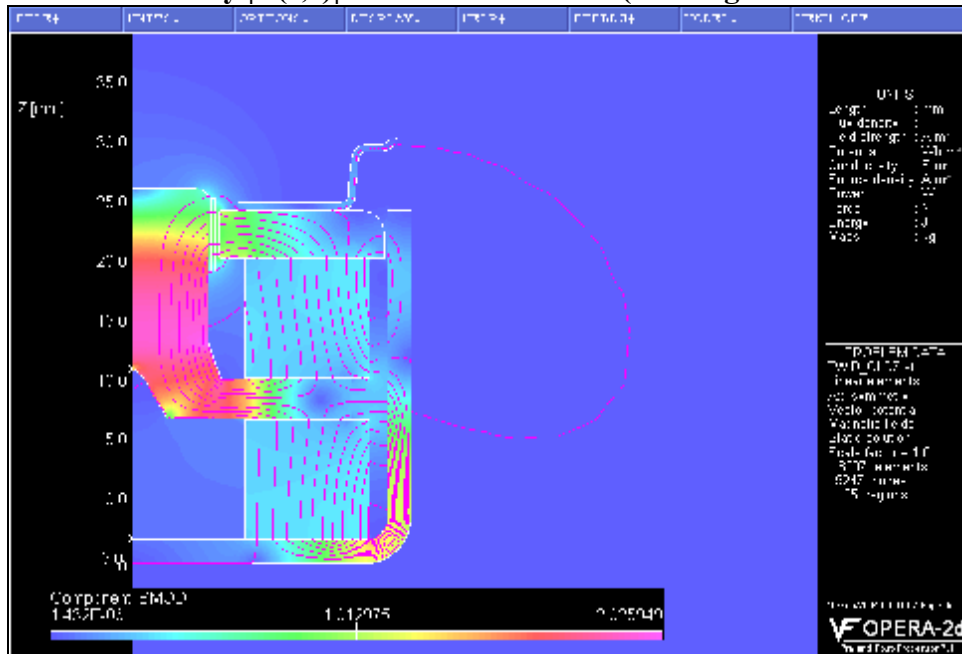


**Figure 5. Contour Plot of the Nonlinear DC Static Finite Element Model Solution for a Typical Magnetically Shielded Small Motor Assembly.**

The typical motor assembly’s DC solution illustrated above utilizes the same magnet for the primary and secondary magnets. The front plate is extended beyond the outside diameter of the primary magnet and has just slightly less of an outside diameter relative to the inside diameter of the shield can. This is done

for predictable shielding and secondary magnet/shield can subassembly-gauging purposes; however, this approach essentially short circuits the motor assembly. This geometry will assure good magnetic shielding, but as we shall see, it is not the most efficient design approach. We could say that this approach is the ‘easy way out’.

Let’s sweep our voice coil through the magnetic gap to evaluate the DC force factor verses voice coil position,  $\mathbf{Bl}(z)$ .

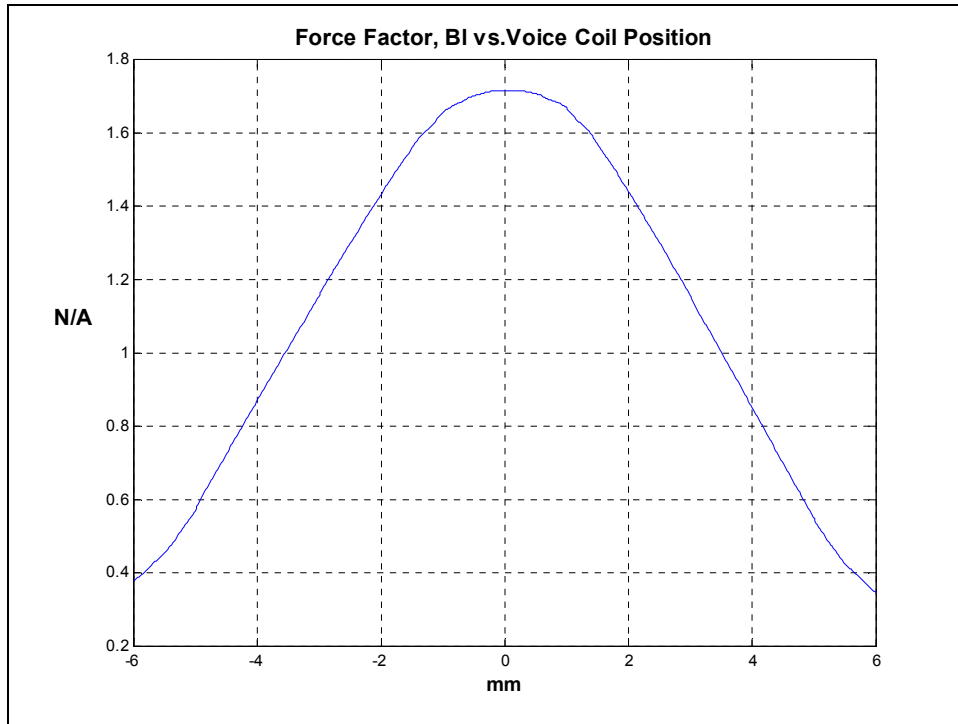


**Figure 6. Results of the Bl.comi Command File inside the DC FEM.**

Although this design looks quite good, we can improve the motor’s DC efficiency quite easily by making changes in the motor assembly geometry. Without the aid of finite element analysis and the appropriate command files, the results of such changes are difficult or impossible to consistently predict.

In figure 5, the DC flux lines are overdrawn onto the contour plot of the magnitude of the  $\mathbf{B}$  field and shows that the losses from both magnets are high. Many of the DC flux lines simply loop around to the shield can from the magnets. We need to push more flux through the magnetic gap. Let’s try to reduce these losses indicated by the flux lines’ loop paths. Figure 7 illustrates an improved motor design that utilizes similar but more practical and efficient geometry. We can reduce the number of flux lines that loop to the shield can from the magnets and therefore the gap efficiency will be increased. The magnets selected are available from several Asian suppliers and are ‘tooled’.

## Magnetic Flux Density $|B(r,z)|$ with the Flux Lines ( $r \times$ Magnetic Vector Potential)

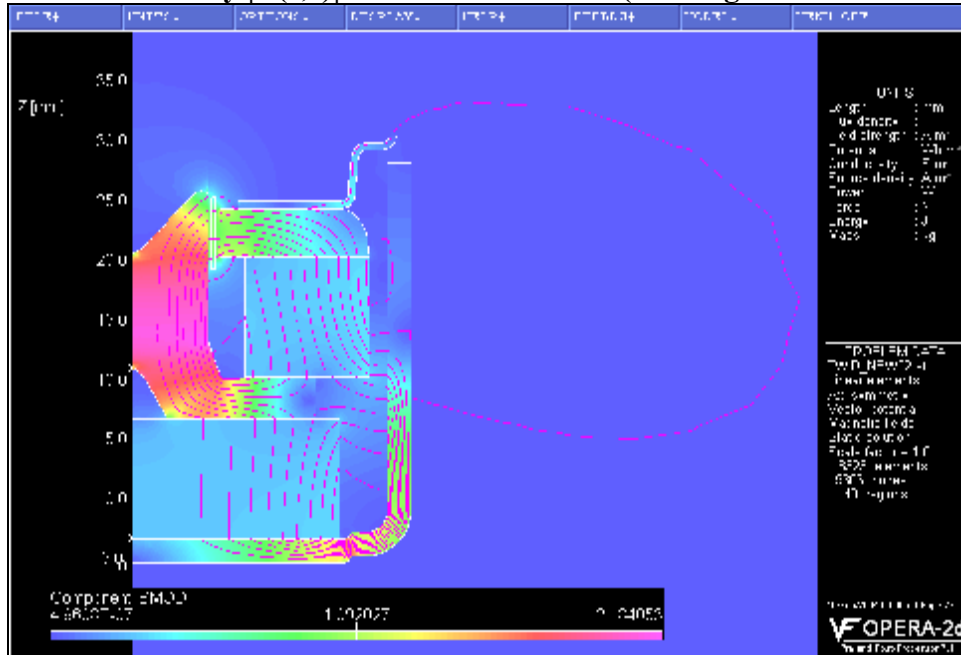


**Figure 7. Contour Plot of the Nonlinear DC Static Finite Element Model Solution for the New Motor Assembly.**

Let's again sweep the voice coil through the magnetic gap and compare the results of  $B(z)$  for both designs. The results of the Bl.comi command file are illustrated in Figure 8 shown below. The new design results in a 15% increase in  $B(0)$  in comparing the new to the old. If we assume that the additional transducer assembly parts are the same, this indicates more than 1 dB in voltage sensitivity of the new design as compared to the old design and a reduction in  $Q_{ts}$  of 30% in the new design, assuming  $Q_{ts} \approx Q_{es}$ . We accomplished this by implementing the following:

1. Reducing the outside diameter of the front plate such that the gap between the front plate and shield can is greater the magnetic gap;
2. Reducing the outside diameter of the back plate;
3. Substituting a cylindrical magnet for a ring magnet of approximately the same volumes;
4. Increasing the height of the shield can;
5. Reshaping the pole tip to pinch and increase the flux density in the vicinity of the magnetic gap.

We start to see the power of the electromagnetic FEA. Using FEA to solve electromagnetic problems builds intuition. We can then use that intuition to work quickly to converge on a new motor design solution(s). Some of the variables that we shall simulate and investigate cannot be measured by practical and/or available measurement systems. Let's keep working. We have much to do.

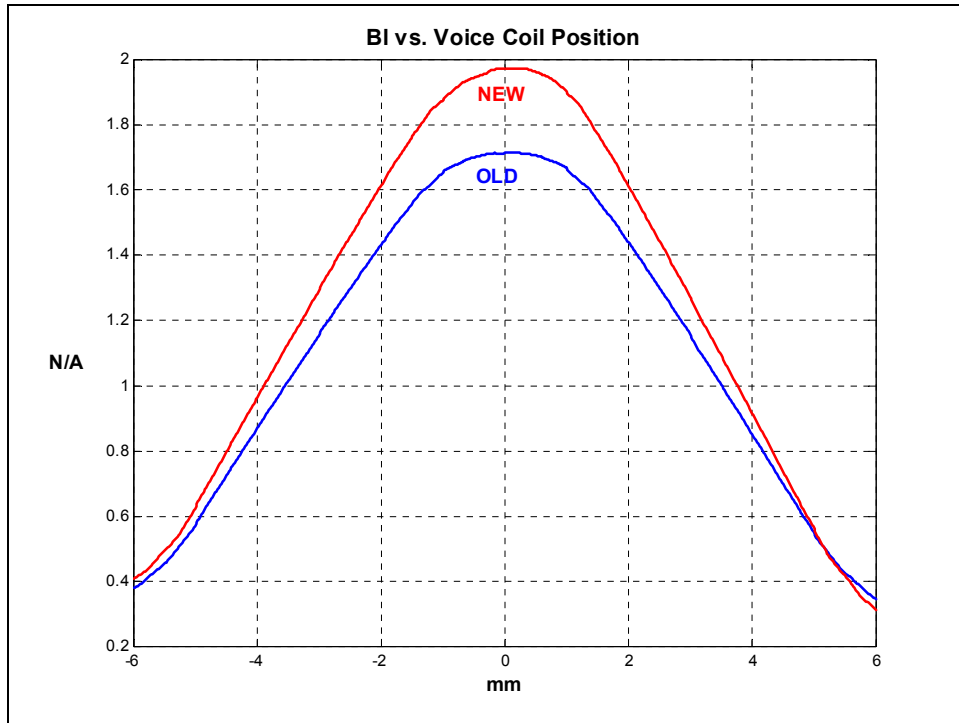


**Figure 8. Command file results of  $BI$  vs. Voice Coil Position for the OLD and NEW motor assembly geometries.**

Based on  $0.82BI(0) \approx BI(\pm 2)$ , we will assume that  $X_{max} \approx 2.0$  mm peak for both designs. This will result in approximately 10% distortion at  $\pm 2$  mm displacements. However, the new design will require less power input for the equivalent displacement due to the increased force factor. There will be an increase in distortion as the displacement is increased beyond  $X_{max}$  in both designs. This is related to the voice coil wind height and the effective magnetic gap height. Increasing the voice coil's wind height could increase  $X_{max}$ ; however, this will typically result in reduced  $BI$  and/or an increase in voice coil mass. One of the major objectives of this article is to compare two designs in a meaningful and informative manor, apples to apples, as much as is possible. This should help to illustrate what is being done during the design process and why. There are an infinite number of solutions. We shall use the same voice coil in all motor assemblies for evaluating the DC and the AC behavior of all the motor assembly models.

Lets now compare the far field  $|\mathbf{B}|$  for the two designs by examining the contour plots illustrated in figures 9 and 10 below. We can determine how well the two designs are magnetically shielded.

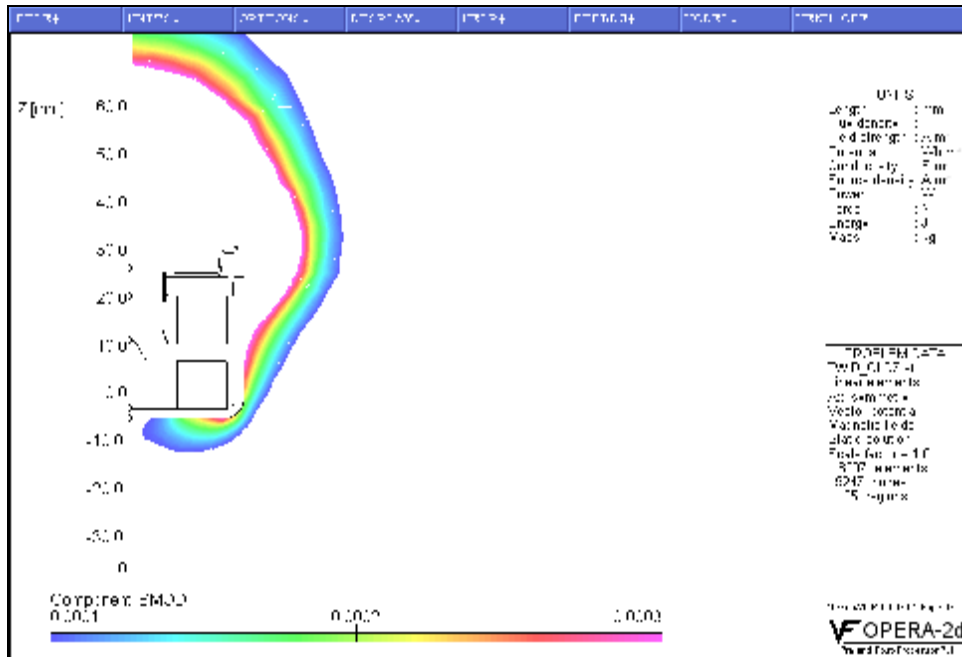


**Figure 9. Contour Plot of the Far Field of  $|\mathbf{B}(r,z)|$  for the Old Design.**

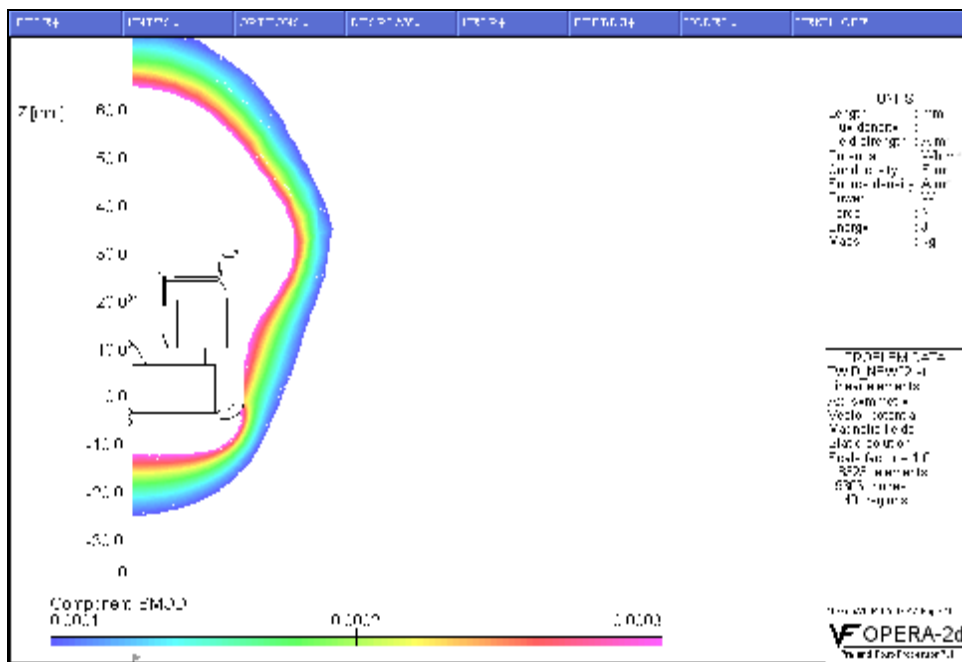


**Figure 10. Contour Plot of the Far Field of  $|\mathbf{B}(r,z)|$  for the New Design.**

The results are very similar with respect to the Flux Density leakage at the side of each design and both are within the 1.0 Gauss at 3 cm measured radially from the outside diameter of the transducer. This is the typical standard for shielded motors and represents a very low value of flux leakage from the motor assemblies. Notice that the new design has slightly less leakage from the front, while the old design has less leakage from the rear of the motor assembly. Both designs are well shielded.

Now let's look at the robustness of each design. This refers to the operating point of both the primary and secondary magnets. Where are we on that BH curve for these magnets

that is illustrated in figure 2 relative to position within the magnets? The higher up on the curve the better. The next four figures, 11, 12, 13, and 14, illustrate the flux density inside the magnets of the old and new motor assembly geometries respectively. We shall clearly see that this quantity varies with position and is not constant in any motor assembly design.

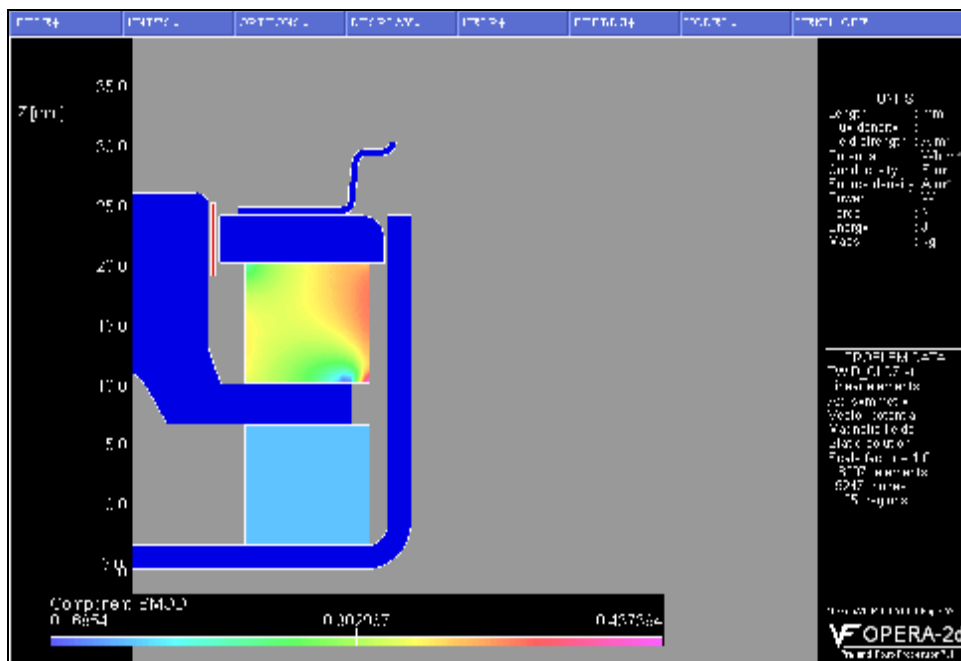


Figure 11. Contour Plot of the  $|B|$  in the Primary Magnet of the Old Geometry.

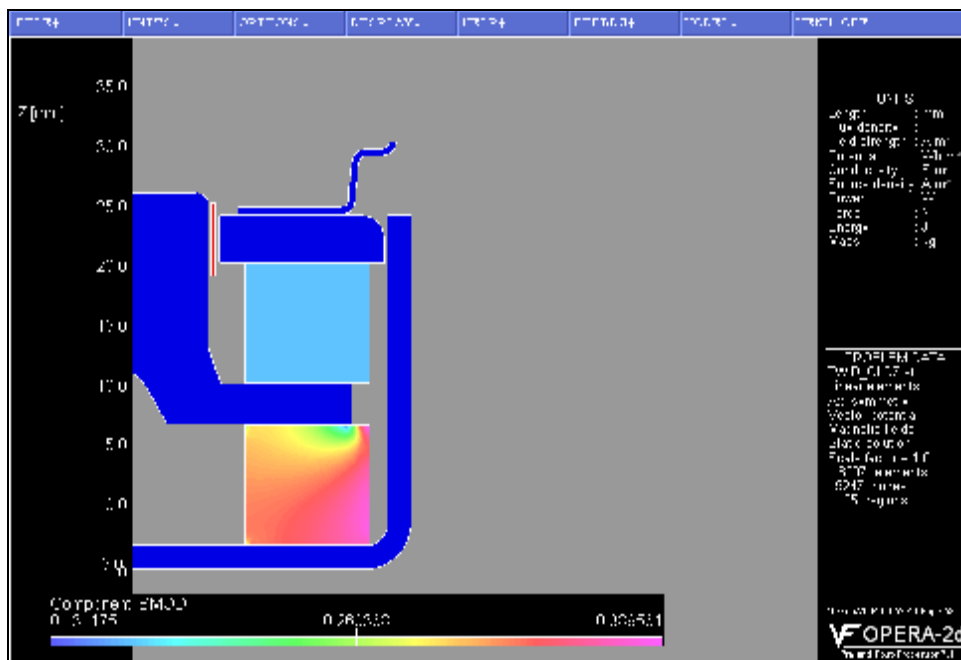


Figure 12. Contour Plot of the  $|B|$  in the Secondary Magnet of the Old Geometry.

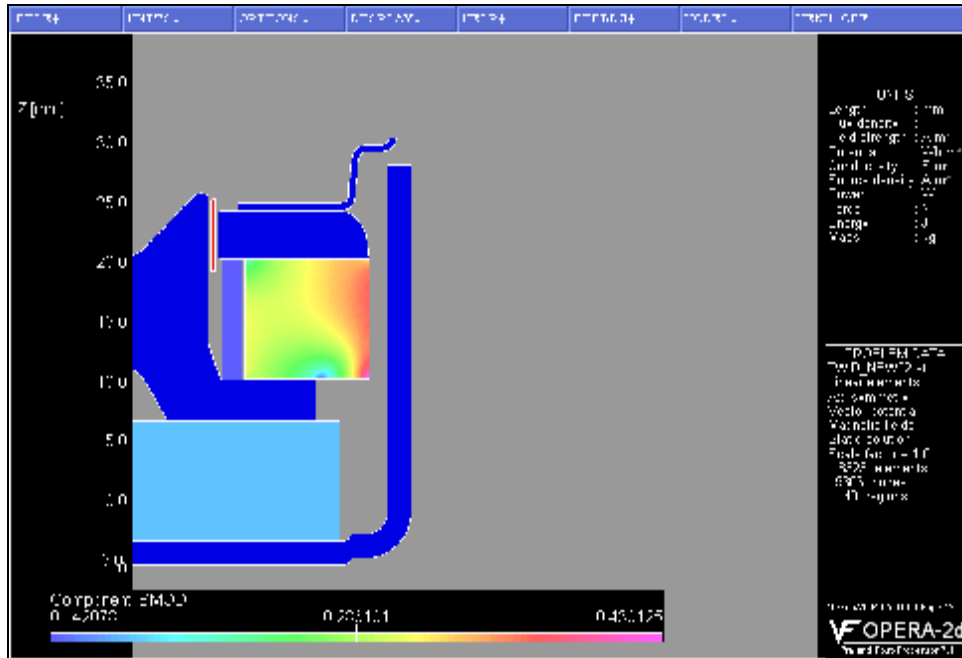


Figure 13. Contour Plot of the  $|B|$  in the Primary Magnet of the New Geometry.

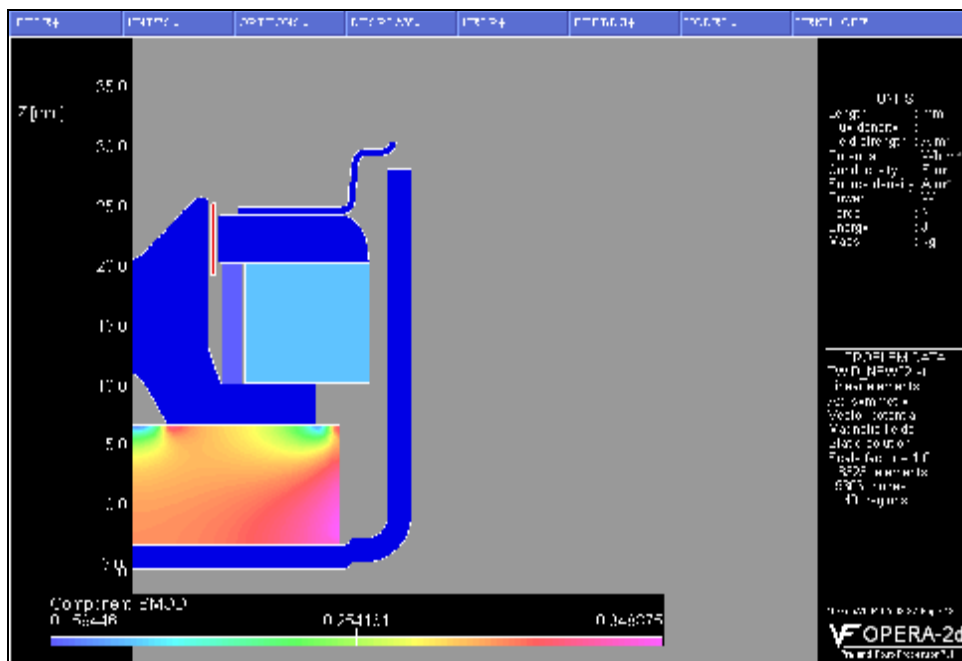


Figure 14. Contour Plot of the  $|B|$  in the Secondary Magnet of the New Geometry.

Both designs are robust and should withstand  $-30$  to  $-40$  °C without irreversible demagnetization. Essentially, because the magnets are quite thick relative to their radial surface area and the magnetic gap width is small and reasonably tall. We must look close to see that the secondary ring magnet in the old design actually has 1% more volume and radial surface area than the cylindrical secondary magnet in the new design; although, the cylindrical magnet appears to be larger by mass and volume. It is not. Please keep in mind that these are axi-symmetric models that are revolved  $360$  ° ( $2\pi$  radians) about the z-axis to calculate the solutions.

## AC ANALYSIS

We have simulated the DC solutions to the two motor assemblies; however, what happens when we apply an AC signal to the voice coil? First we must enter the electrical conductivity material property of

1010 steel, Ceramic 8, copper, and air. Figure 15 illustrates the induced AC eddy current density and figure 16 illustrates the induced AC magnetic  $\mathbf{B}$  field at 100 Hz. Both are a result of the input current density applied to the voice coil and the resultant electric field associated with the voice coil, which induce an eddy current density within the motor assembly. All restart nonlinear AC finite element analysis was performed with an input AC current density of  $10^6 \text{ Am}^{-2}$  within the voice coil.



**Figure 15. Contour Plot of the Induced Eddy Current Density in the Old Motor Assembly at 100 Hz.**

Ampere’s Law tells us that where there is current; there is a magnetic field. Figure 16 illustrates a small AC induced flux density,  $|\mathbf{B}(\mathbf{r},\mathbf{z})|$ , with a peak value of 0.022 T.

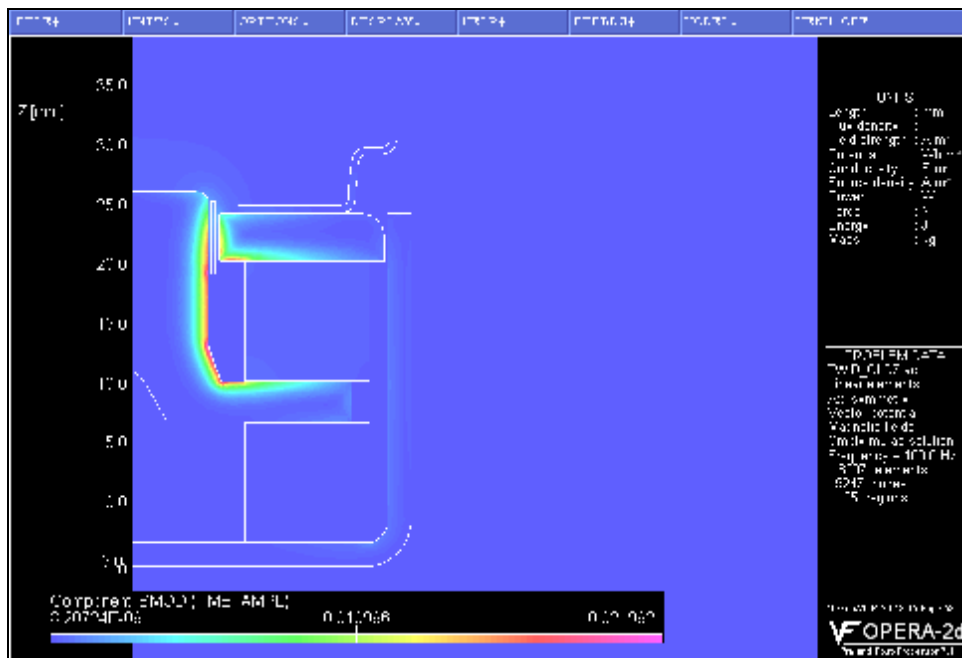


**Figure 16. Contour Plot of the Magnitude of the AC Induced B Field for the Old Motor Assembly.**

Where there is magnetic flux density,  $\mathbf{B}$ , there are flux lines. Figure 17 illustrates the AC flux lines’ paths in the AC finite element model of the old motor assembly.

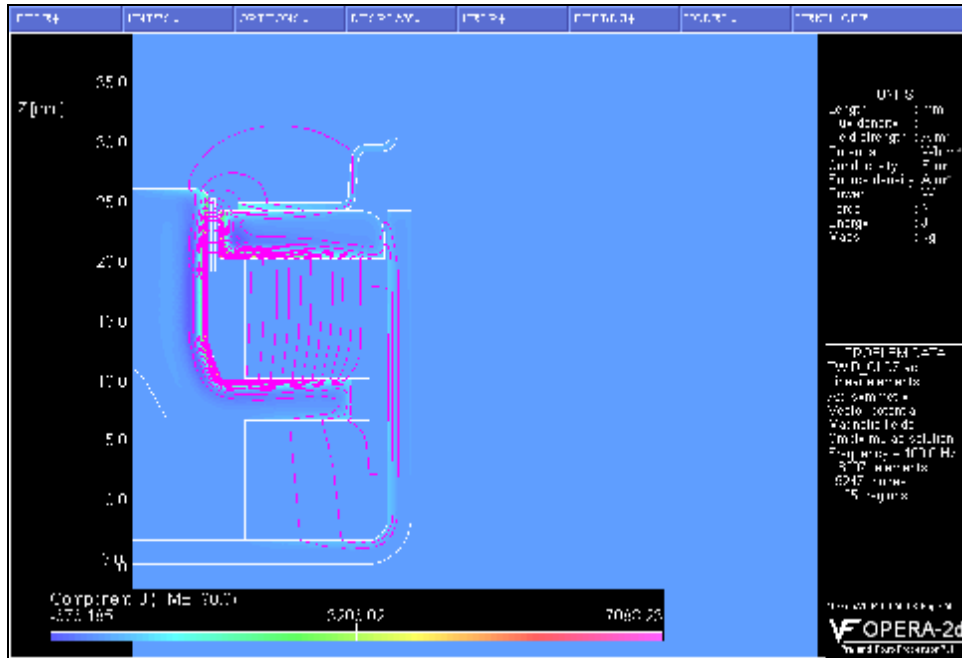


**Figure 17. Contour Plot of the Induced AC Flux Lines in the Old Motor Assembly at 100 Hz.**

We can see that in this model the AC flux lines follow similar paths to the DC flux lines. Let's now look at the new motor assembly with the addition of a copper-shorting (cheating) ring between the primary magnet's inside diameter and the pole piece. Typically, a thin copper cap is pressed over the pole piece's outside diameter to control the AC affects. In most cases this works quite well in controlling the induced AC phenomenon within the motor assembly; however, the magnetic gap efficiency and operating points of the magnets are reduced in a DC sense.



**Figure 18. Contour Plot of the Induced Eddy Current Density in the New Motor Assembly at 100 Hz.**

Figure 19 shows that we still have an induced magnetic field with the copper shorting ring; however, the peak value has been reduced to 0.007 T, less than one third of the previous model.

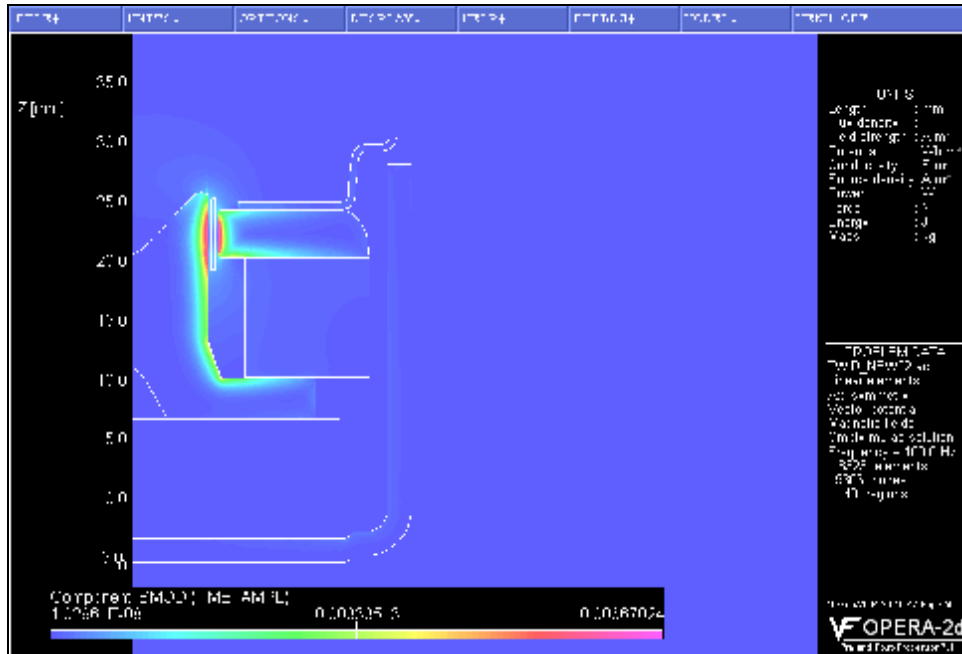


Figure 19. Contour Plot of the Magnitude of the AC Induced B Field for the New Motor Design.

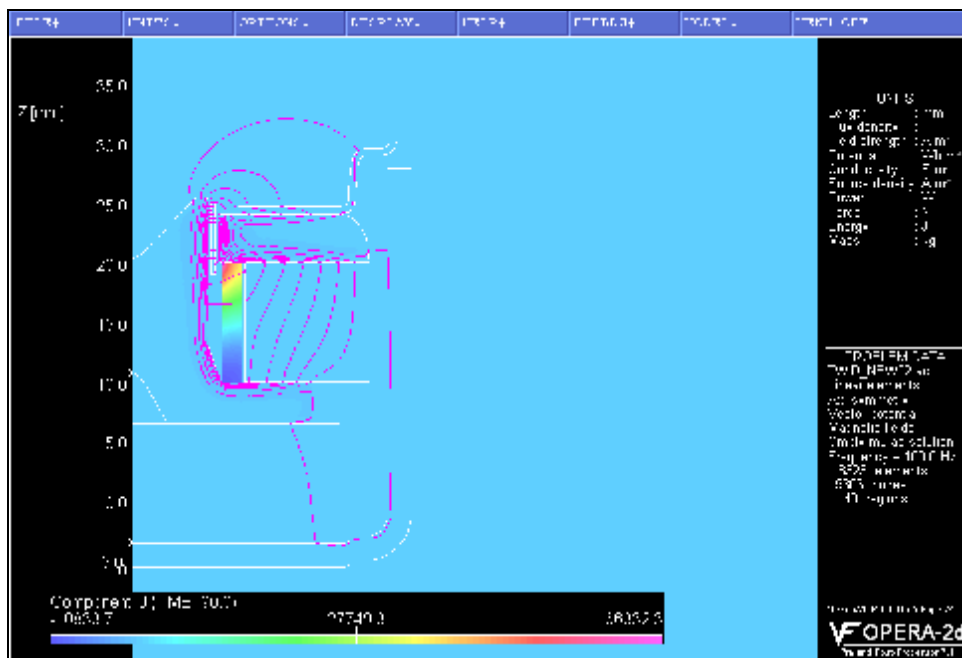


Figure 20. Contour Plot of the Induced AC Flux Lines in the New Motor Assembly at 100 Hz.

We can clearly see that there are significant differences in the behavior of these two motor assemblies with regards to the induced AC eddy current density and the AC magnetic field. In the new design, the induced AC eddy current density is essentially contained within the high electrical conductivity material, copper, while the AC flux lines loop around the magnetic gap and follow very different paths than the DC flux lines. The low electrical conductivity steel has a very low eddy current density and this is desirable. With the eddy current in the copper, the AC magnetic field will be small due to the low permeability of copper, the same as air. The permeability of copper is the slope of the BH curve in figure 4, where  $B/H = \mu$  and in this case what is referred to as  $\mu_0$ . Likewise the slopes of the BH curve of steel indicate the permeability of the material; however, a line does not define the BH curve for this material. Steel has nonlinear magnetic characteristics. The magnets are a special case and also have a permeability of

$\mu_0$ . Another point to consider is that the AC FEA is restarted from the DC permeability. The DC permeability will indeed have an effect on the AC behavior of the induced magnetic fields. Let's look at the DC permeability of the new motor assembly. Within the steel the permeability is low where the flux density is high and vice versa. Please note that for convenience  $\mu_0$  is indicated as the value 1, where  $\mu = \mu_0 \mu_{rel}$ .



Figure 21. Contour Plot of the Relative DC Permeability for the Restart Nonlinear AC FEA Solutions for the New Motor Assembly.

Let's look at some other higher frequency, 1.0 kHz and 10.0 kHz, contour plots for the new motor assembly.

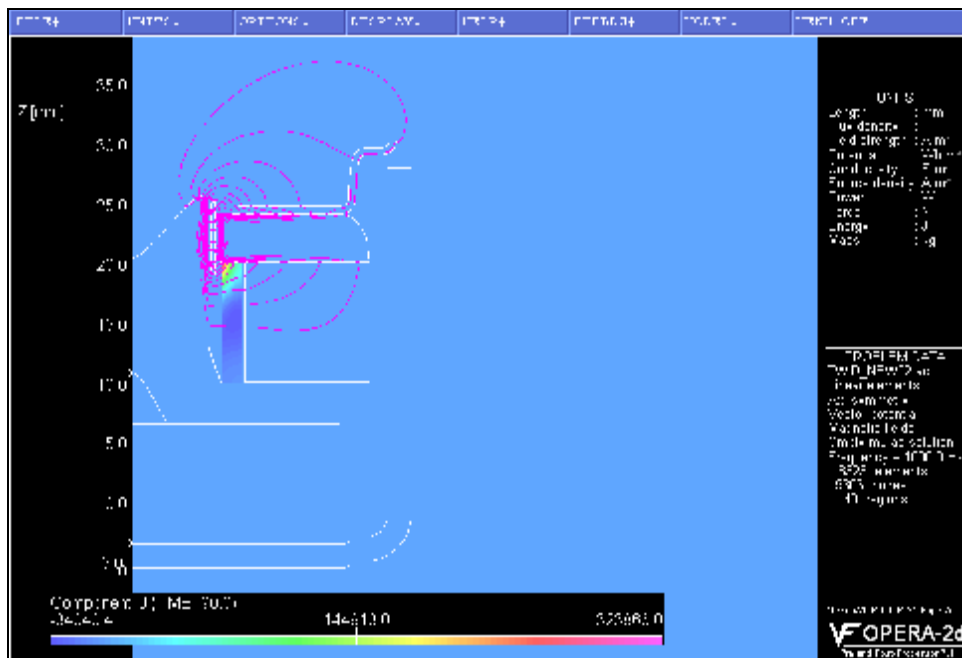
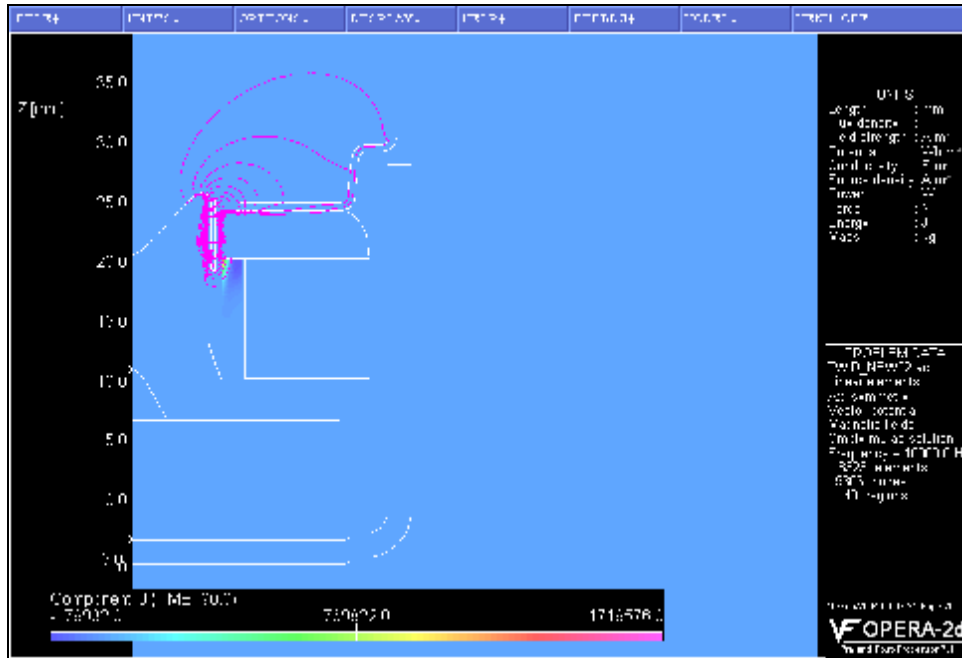
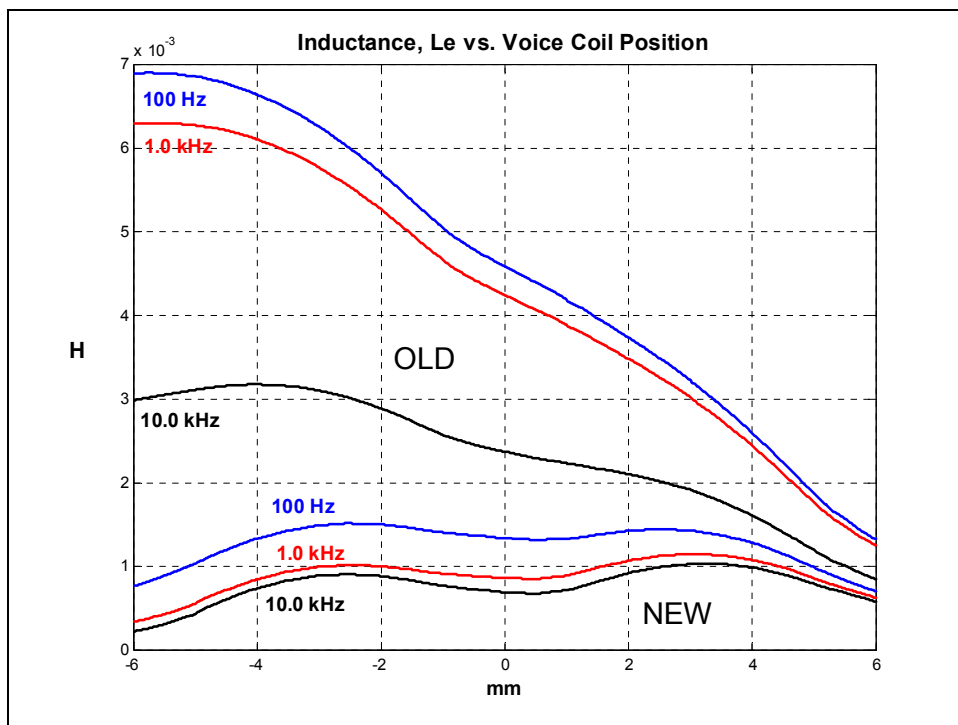


Figure 22. Contour Plot of the Induced AC Flux Lines in the New Motor Assembly at 1.0 kHz.



**Figure 23. Contour Plot of the Induced AC Flux Lines in the New Motor Assembly at 10.0 kHz.**

The looping of the AC flux lines seems to become more symmetrical with respect to the front plate center as frequency is increased. Let's use my AC command file to see how the AC flux lines link to the voice coil. Notice how the old motor design has increasing inductance as the voice coil is displaced into the motor (-z direction). This is a result of a steel core versus an air core inductor with regards to the self-inductance of the voice coil. The contour plots tell it all.



**Figure 24. Results of  $L_e.comi$  within Old and New Motor Assemblies AC FEM.**

Now we can see that the shorting ring reduces inductance and amplitude and frequency modulation of inductance,  $L_e(z, f)$ . There is a linearization and reduction of the self-inductance of the voice coil in the new motor design.

Finally, let's check the induced AC force factor. The AC force factor, although small, can induce a DC offset in the voice coil's zero position that is dependant on frequency and drive level.

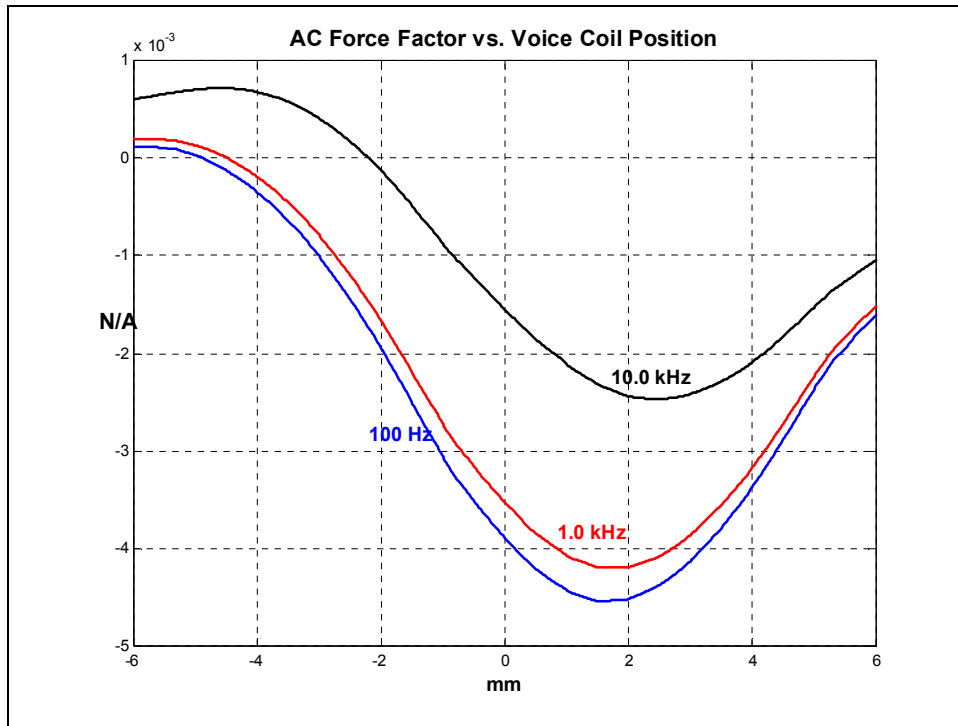


Figure 25. Plot of the AC Force Factor vs. Voice Coil Position for Old Motor.

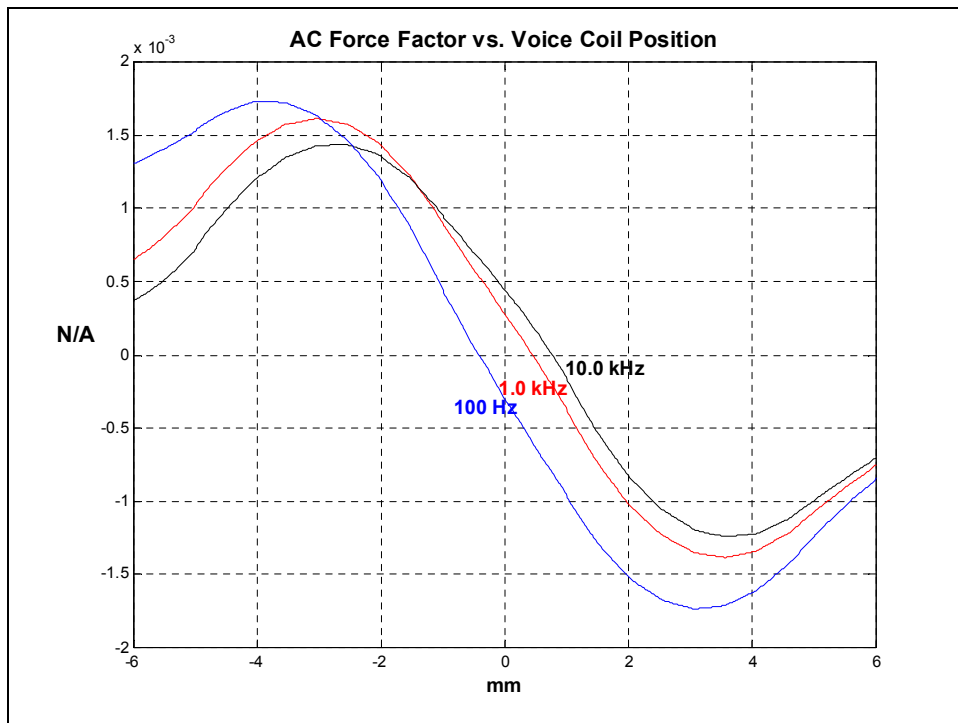


Figure 26. Plot of the AC Force Factor vs. Voice Coil Position for New Motor.

In comparing the command file results, it is illustrated that the new motor's AC force factor is much more symmetrical about the zero voice coil, rest, position and the amplitude has been reduced. Notice that over the displacement range of  $\pm 2.0$  mm, the AC force factor will modulate with the DC force factor in a fairly linear manor. This is desirable and the probability of an induced DC offset is small. On the other hand, the old motor is sure to have a small induced DC offset that will depend on input

drive level. Again we see that the amplitude and frequency modulation of the AC force factor is reduced in the new motor assembly as a result of the copper-shorting ring..

The resultant linearization of the inductance and the induced AC force factor along with the reduction in amplitude and frequency modulation of the quantities within the new motor assembly will reduce distortion, both IM and THD, to some degree. However, these are actually secondary effects. The shorting ring's main function is to increase bandwidth by reducing the self-inductance of the voice coil. This is clearly illustrated in figure 24.

### THERMAL ANALYSIS

Ok, things look good so far but lets look at what happens to the motor assembly with regards to heat after the motor assembly has reached its steady state operating temperature. We have an AC current density in the aluminum voice coil and an AC eddy current density within the motor assembly. Now we must enter the thermal conductivity material property of, 1010 steel, Ceramic 8, copper, and air and apply the boundary conditions. Let's see how 'hot' things get. Is there any difference in the two designs? Well, let's take a look.

The linear thermal FEA is restarted from the nonlinear AC solution. The DC, AC and thermal FEA solutions are coupled. All material properties are identical except for the copper shorting ring in the new design. The use of heat transfer coefficient boundary conditions control convection cooling within the motor assembly model. The ambient temperature used for the thermal FEA was 25 °C. Figures 17 and 18 illustrate the results of the steady state thermal FEA for the old and new motor designs respectively.

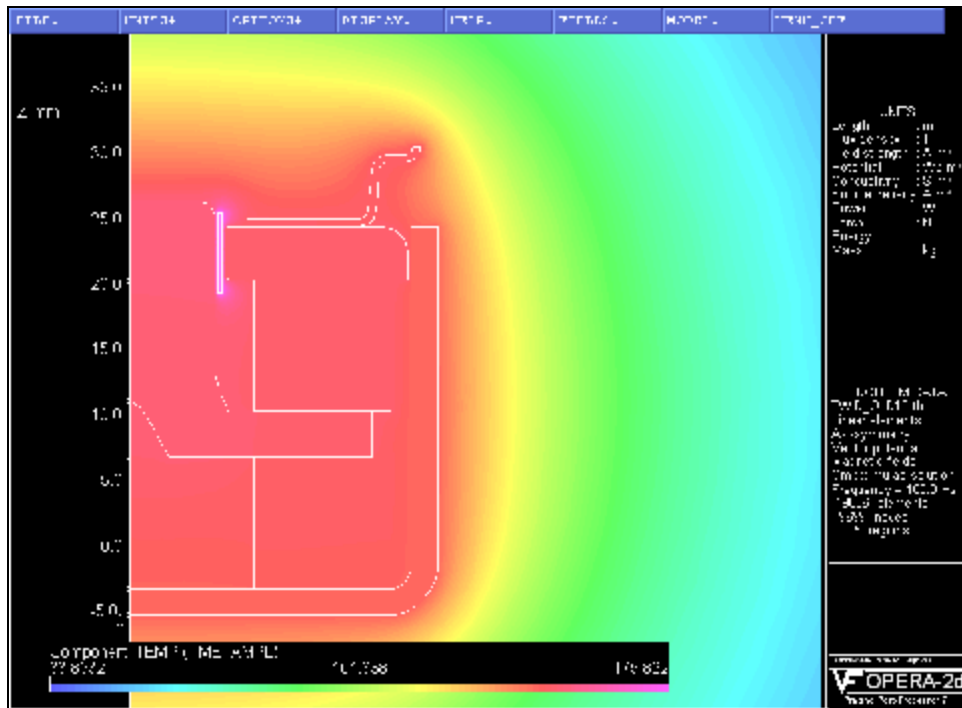
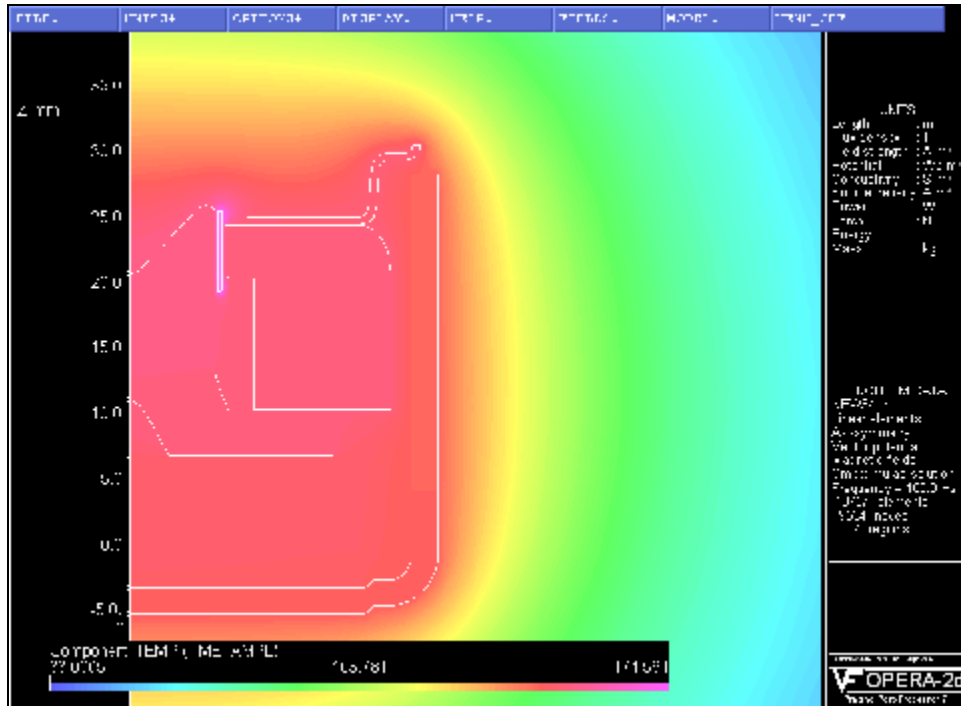


Figure 27. Contour plot of Temperature in °C versus Position for the Old Motor Assembly at 100 Hz with ~10 W<sub>RMS</sub> Input.



**Figure 28. Contour plot of Temperature in °C versus Position for the New Motor Assembly at 100 Hz with ~10 W<sub>RMS</sub> Input.**

The results of the thermal FEA for the two motor assemblies are quite similar and surprisingly inconclusive. Typically, transducer engineers refer to this as ‘a wash’. In these models our concern is with the voice coil operating temperature. However, if we had utilized NEO magnet(s), the thermal FEA would be helpful in simulating the steady state operating temperature of the high temperature sensitive NEO magnet(s).

### **MOTOR ASSEMBLY DRAWING**

It’s DXF out and mirror inside your CAD program. The geometry created within the pre-processor can be exported and utilized as the basis for the motor assembly drawing. Our design simulations are self-documenting. Another consideration is that the exported geometry ‘always’ has its centerline coincident with  $x = 0$ . This is illustrated in figure 29 by the green centerline and is due to the mirroring of the axi-symmetric geometry. Once the geometry is exported it is not advised that you move it. We can build the transducer assembly drawing around the motor sub-assembly, a bottom-up design approach. This is important if we want to subsequently create soft-part geometries for analysis inside of our CAD program. Axi-symmetric FEA only works for zero and positive values of  $x$ , no negative values of  $x$  please.

If we look closely at figure 29, the cross-sectional motor assembly drawing, illustrates that this motor assembly was designed for manufacturability and assembly. The copper-shorting ring is self-aligning and acts as an integral gauge for positioning the primary magnet. The shield can contains a feature that positions the secondary magnet, while three small nylon spot gauges are bonded to the outside diameter of the primary magnet with pre-applied pressure sensitive adhesive. These integral spot gauges align the secondary magnet/shield can subassembly. Additionally, the back plate contains a centering feature to facilitate consistent adhesive dispense during the manufacturing processes. The motor is self-gauging with the exception of a gap (hard-parts) gauge and a voice coil (soft-parts) gauge. It is also shown that the stamped steel basket is positioned and mechanically attached to the motor assembly by four integral rivets as a feature of the front plate. Please do not forget the polyvinyl acetate (PVA) adhesive buzz washer at the basket to front plate interface.

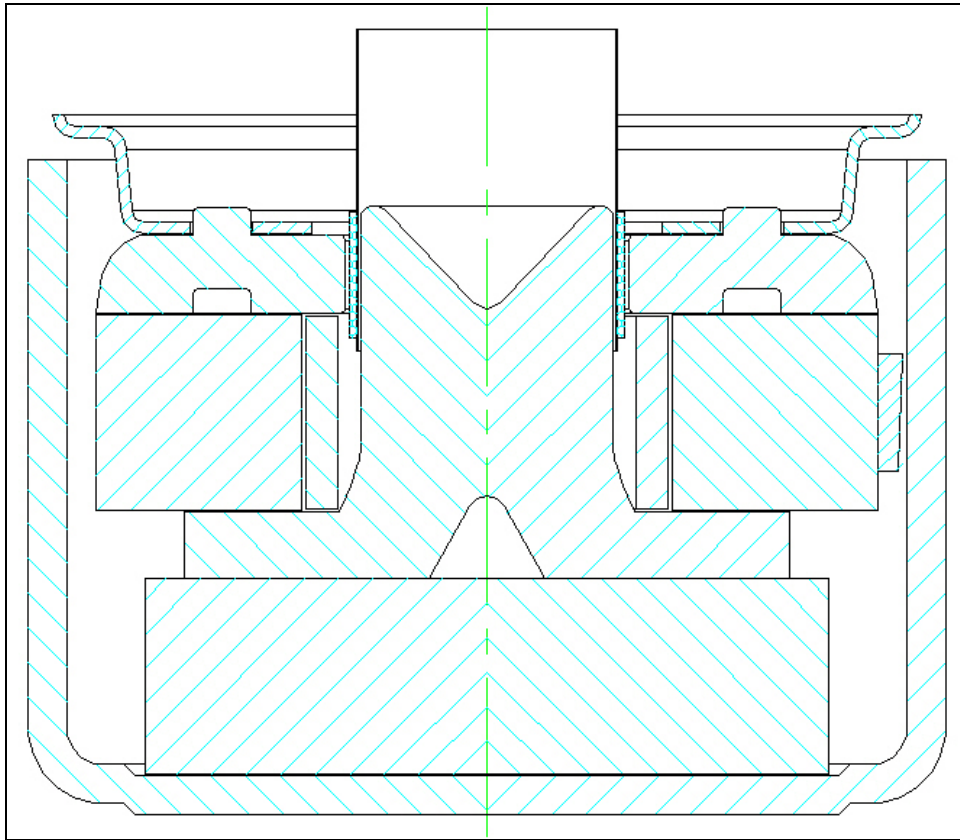


**Figure 29. Sectional Assembly Drawing of the New Motor.**

It has been shown that we can simulate and document the transducer motor assembly quickly and effectively by utilizing the same geometry for DC, AC and thermal finite element models. Computer simulation of motor assemblies can improve transducer performance; reduce development costs; reduce time to market; and help to build a 'body of knowledge' for the transducer engineer. Although this was an example of a small, less than 2.0 in. OD, motor assembly design, the simulation techniques utilized can be applied to larger and/or smaller transducer motor assembly designs.

That's the Phuket Report.

Steve Mowry

[stephen\\_mowry@hotmail.com](mailto:stephen_mowry@hotmail.com)